# ASTER spectral analysis and lithologic mapping of the Khanneshin carbonatite volcano, Afghanistan

**John C. Mars* and Lawrence C. Rowan†**
*U.S. Geological Survey, MS 954, Reston, Virginia 20192, USA*

## ABSTRACT

**Advanced Spaceborne Thermal and Reflection Radiometer (ASTER) data of the early Quaternary Khanneshin carbonatite volcano located in southern Afghanistan were used to identify carbonate rocks within the volcano and to distinguish them from Neogene ferruginous polymict sandstone and argillite. The carbonatitic rocks are characterized by diagnostic $CO_3$ absorption near 11.2 μm and 2.31–2.33 μm, whereas the sandstone, argillite, and adjacent alluvial deposits exhibit intense Si-O absorption near 8.7 μm caused mainly by quartz and Al-OH absorption near 2.20 μm due to muscovite and illite.**

**Calcitic carbonatite was distinguished from ankeritic carbonatite in the short wave infrared (SWIR) region of the ASTER data due to a slight shift of the $CO_3$ absorption feature toward 2.26 μm (ASTER band 7) in the ankeritic carbonatite spectra. Spectral assessment using ASTER SWIR data suggests that the area is covered by extensive carbonatite flows that contain calcite, ankerite, and muscovite, though some areas mapped as ankeritic carbonatite on a preexisting geologic map were not identified in the ASTER data. A contact aureole shown on the geologic map was defined using an ASTER false color composite image (R = 6, G = 3, B = 1) and a logical operator byte image. The contact aureole rocks exhibit $Fe^{2+}$, Al-OH, and Fe, Mg-OH spectral absorption features at 1.65, 2.2, and 2.33 μm, respectively, which suggest that the contact aureole rocks contain muscovite, epidote, and chlorite. The contact aureole rocks were mapped using an Interactive Data Language (IDL) logical operator.**

**A visible through short wave infrared (VNIR-SWIR) mineral and rock-type map based on matched filter, band ratio, and logical operator analysis illustrates: (1) laterally extensive calcitic carbonatite that covers most of the crater and areas northeast of the crater; (2) ankeritic carbonatite located southeast and north of the crater and some small deposits located within the crater; (3) agglomerate that primarily covers the inside rim of the crater and a small area west of the crater; (4) a crater rim that consists mostly of epidote-chlorite-muscovite–rich metamorphosed argillite and sandstone; and (5) iron ($Fe^{3+}$) and muscovite-illite–rich rocks and iron-rich eolian sands surrounding the western part of the volcano. The thermal infrared (TIR) rock-type map illustrates laterally extensive carbonatitic and mafic rocks surrounded by quartz-rich eolian and fluvial reworked sediments. In addition, the combination of VNIR, SWIR, and TIR data complement one another in that the TIR data illustrate more laterally extensive rock types and the VNIR-SWIR data distinguish more specific varieties of rocks and mineral mixtures.**

## INTRODUCTION

Carbonatites are of economic importance due to their typical association with deposits of rare earth and radioactive elements (Alkhazov et al., 1978; Castor, 1991; Le Bas, 1977; Olson et al., 1954). Carbonatite deposits consist of carbonate-rich rocks that contain diagnostic spectral absorption features (Rowan et al., 1984; Rowan et al., 1986; Rowan, 1997). The rarity and unique spectral characteristics of carbonate-rich carbonatites dictate the need for spectroscopic remote sensing analysis and mapping of surfical deposits, which will aid future exploration and research.

The Khanneshin carbonatite volcano is located in the Registan Desert ~240 km southwest of Kandahar, Afghanistan (Fig. 1). According to Alkhazov et al. (1978), the volcano formed during the early Quaternary period as multiple episodes of carbonatite volcanogenic and volcanogenic-sedimentary facies formed a domelike base with a superimposed cone, as well as numerous "explosion pipes" (Fig. 2). Alkhazov et al. (1978) also note the presence of rare-earth-element- (REE) rich zones and concentrations of phosphorus, iron, strontium, and radioactive minerals. The diameter of the dissected volcano is ~10 km (Alkhazov et al., 1978). The cone stands ~700 m above the desert floor, and a 2.1 km × 3.1 km caldera occupies the central part (Fig. 1B). In this study, an Advanced Spaceborne Thermal Emission and Reflection Radiometer (ASTER) false color composite image (R = 6, G = 3, B = 1) is used to define the caldera (crater) as the area within a circular pattern of green pixels (dotted line, Fig. 1B).

ASTER measures reflected radiation in three bands between 0.52 and 0.86 μm (VNIR); in six bands from 1.65 to 2.43 μm (SWIR); and emitted radiation in five bands in the 8.125–11.65 μm wavelength region (TIR) with 15 m, 30 m, and 90 m resolution, respectively (Fujisada, 1995). ASTER also has a back-looking VNIR telescope with 15 m resolution. Thus, stereoscopic VNIR images can be acquired at 15 m resolution. The swath-width is 60 km, but ASTER's off-nadir pointing capability extends the total cross-track viewing capability to 232 km (Fujisada, 1995).

The purpose of this study is to evaluate data recorded by the ASTER imaging system for mapping the Khanneshin volcano lithologies, especially the carbonatitic deposits with which potentially important mineral deposits appear to be associated. The study area includes the volcanic crater, surrounding flows, and alluvial and desert-plain deposits (Fig. 1B). This evaluation is based on comparison of image analysis results to a generalized geologic map (Fig. 2; Alkhazov et al., 1978). In addition, interpretation of the images is based on previous documentation of the spectral reflectance and spectral emittance of carbonatites and associated alkalic rocks collected from other sites such as Mountain Pass, California and Iron Hill, Colorado (Bowers and Rowan, 1996; Rowan, 1997;

*Email: jmars@usgs.gov.
†Deceased 05/02/2010.

*Geosphere*; February 2011; v. 7; no. 1; p. 276–289; doi: 10.1130/GES00630.1; 17 figures.

Rowan, 1998; Rowan et al., 1984; Rowan et al., 1986; Rowan et al., 1995; Rowan and Mars, 2003; Watson et al., 1996).

## GEOLOGY

The initial phase of formation of the Khanneshin volcano was the shallow intrusion of sovite and doming of red, ferruginous polymict sandstone and argillite (Alkhazov et al., 1978) (Fig. 2). Subsequently, the dome was breached by extrusion of gray, banded breccialike strontianite sovite, which consists mainly of calcite and strontianite, and minor acmite, barite, biotite, phlogopite, apatite, and pyrochlore (Alkhazov et al., 1978) (Fig. 2). The main crater was nearly filled with barite-calcite-ankerite agglomeratic deposits of the next phase, which also contain magnetite, phlogopite, apatite, acmite, fluorite, REE-carbonate minerals, galena, and pyrochlore (Fig. 2). Most of the subsequent volcanism was characterized by carbonatitic diatremes, the largest of which is 500 × 900 m, and alvikite lava and volcanic-sedimentary rocks mainly within the main crater (Alkhazov et al., 1978) (Fig. 2). The diatreme deposits and alvikite lava contain abundant xenoliths and nodules consisting of calcite, clinopyroxene, biotite, garnet, magnetite, apatite, melilite, phlogopite, analcime, and fenite (Alkhazov et al., 1978). The carbonatitic rocks are grouped into two units, dominantly calcitic tuffs, lavas, and agglomerates (carb1—yellow, Fig. 2) and dominantly ankeritic lavas, tuffs, and agglomerate (carb2—green, Fig. 2). Volcanic-sedimentary rocks are common in the calcitic and ankeritic carbonatitic units (carb1 and carb2, Fig. 2).

Carbonatite dikes and veins are also characteristic of the later stages of activity. The terminal phase of activity at the Khanneshin volcano was extrusion of leucite phonolite lava in the

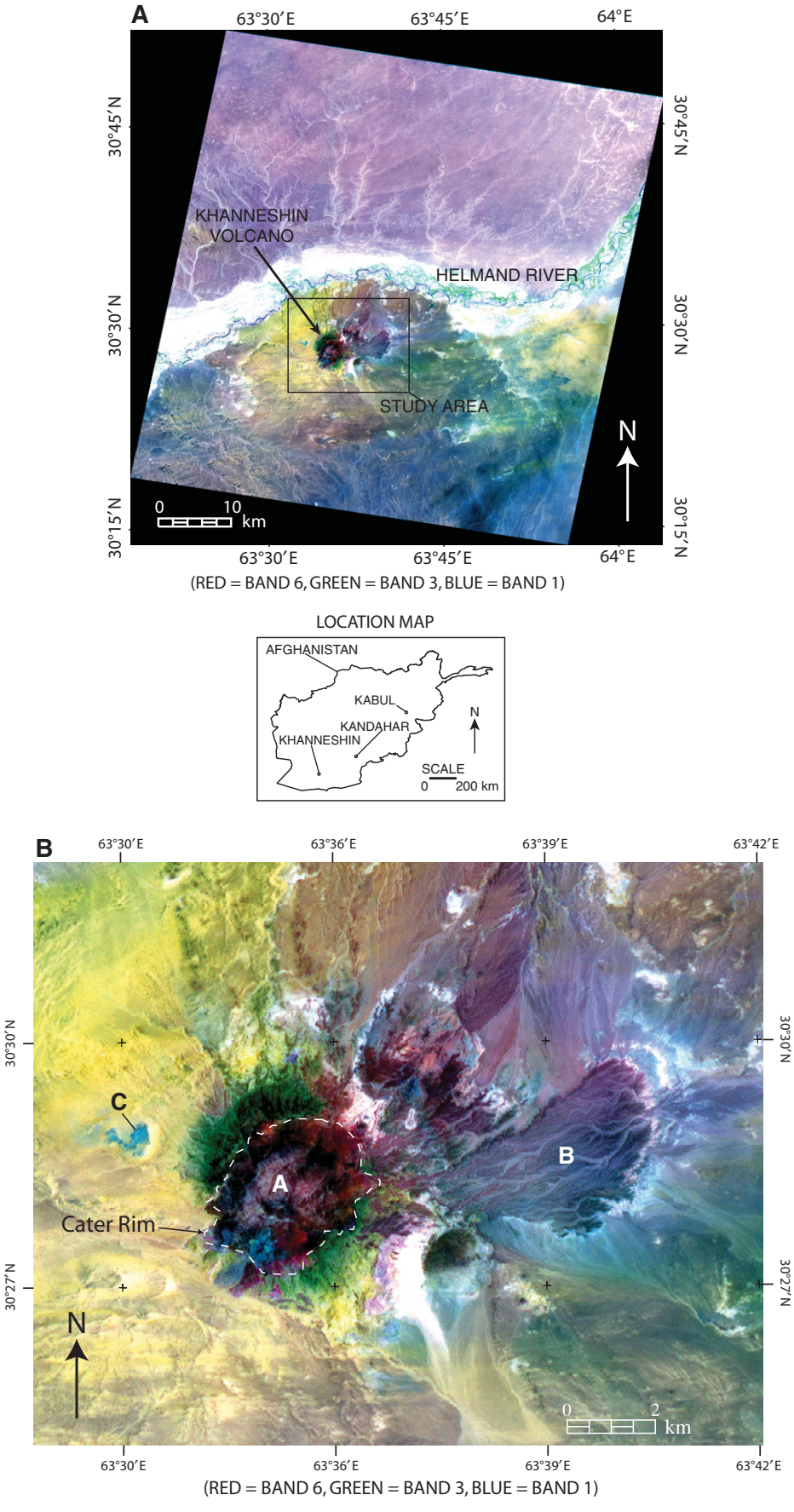


**Figure 1. (A) ASTER false-color composite image (red—band 6; green—band 3; and blue—band 1) of the Registan, Afghanistan, area showing the Khanneshin volcano and location of the study area south of the Helmand River (solid line). (B) ASTER subset false-color composite image (red—band 6; green—band 3; and blue—band 1) of the study area showing the location of the Khanneshin crater—A, crater rim (dotted line) highlighted by green colored rocks, and large fluvial terrace deposit—B. Additional volcanic deposits flank the north, northeast, and southeast rim of the crater. An isolated volcanic deposit is located west of the volcano—C.**

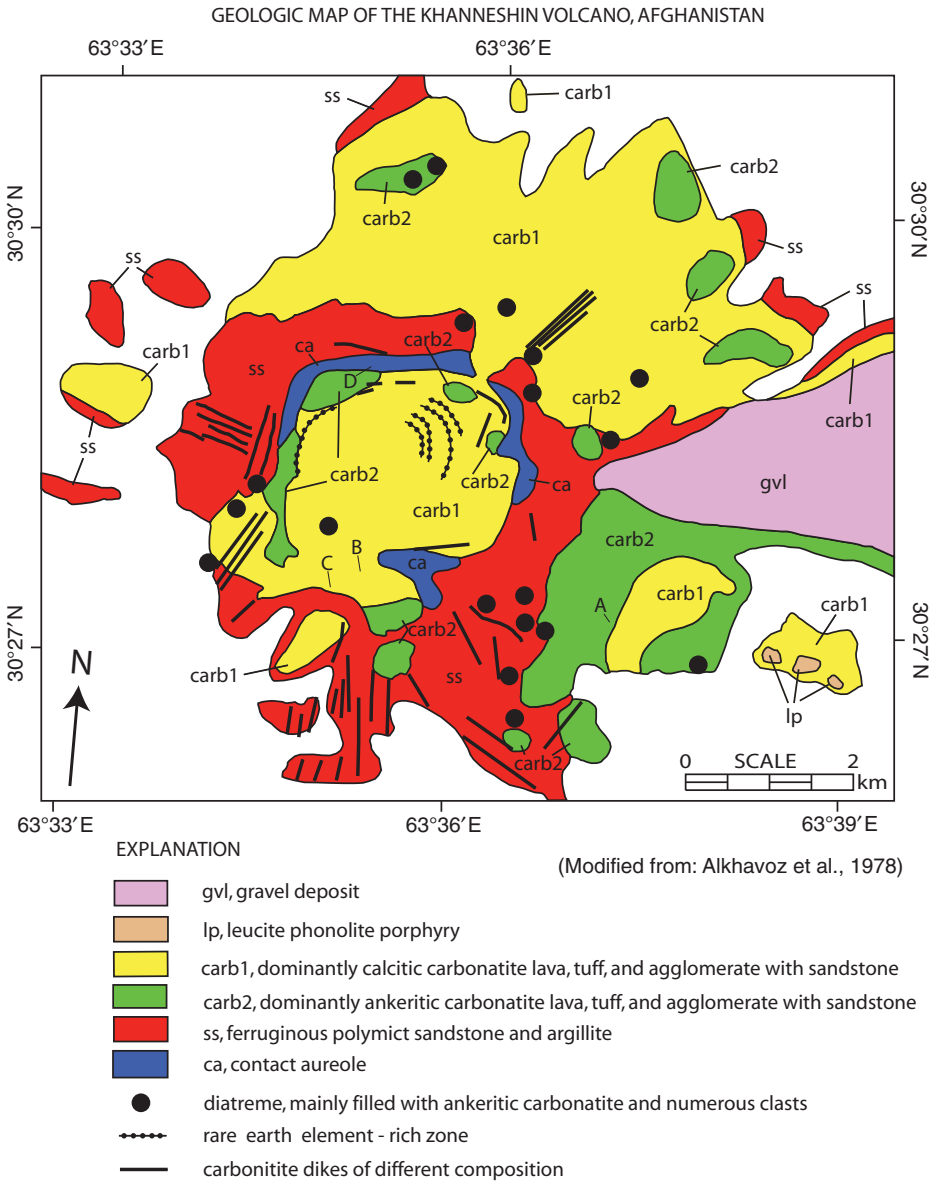


**Figure 2. Generalized geologic map of the Khanneshin, Afghanistan volcano and surrounding area (modified after Alkhazov et al., 1978). A—Location of ankeritic spectral endmember. B—Location of calcitic carbonatite spectral endmember. C—Location of agglomerate spectral endmember. D—Location of muscovite spectral endmember.**

southeastern sector, which is the only alkaline volcanic rock associated with these carbonatite deposits (lp, Fig. 2). Erosion of the volcano resulted in the "Upper Pliocene gravel-rubble, proluvial deposits" (gvl, Fig. 2). Note that the barite-ankerite carbonatite lavas and tuffs and Neogene polymict sandstone and argillite are exposed along the fan margin (carb1 and ss, respectively, Fig. 2).

Contact metamorphism resulted in a 5–100-m-wide band of greenish rocks around the crater periphery, which Alkhazov et al. (1978) reported being enriched in phosphorous. They also reported REE-carbonate minerals, including bastnaesnite and burbankite, concentrated in hydrothermally altered rocks in the southwestern part of the volcano, in addition to those REE zones indicated within the crater (Fig. 2).

## CARBONATITE SPECTRAL CHARACTERISTICS

The spectral characteristics of carbonatitic rocks are dominated by carbonate minerals, but in some deposits silicate minerals and certain oxide-minerals have significant effects (Rowan et al., 1984; Rowan et al., 1986; Rowan et al., 1995). Carbonate mineral laboratory spectra are distinctive in the 8–12 µm thermal infrared (TIR) region because of the presence of a weak absorption feature near 11.2 µm and, otherwise, generally flat spectra (Fig. 3A). This weak feature is evident as a slight drop in emittance in band 14 in ASTER TIR spectra due to the breadth of the TIR bandpasses (Fig. 3B). As noted in the geologic description of the study area, a wide range of other minerals is common in carbonatite, and absorption features exhibited by them cause departure from the generally flat emittance spectrum (Fig. 3A). Note that some rock-forming minerals exhibit important absorption features near 10.0 µm in laboratory spectra, but ASTER does not have a band in this region due to atmospheric absorption. Nevertheless, spectra of mafic minerals, such as biotite, hornblende, and epidote, display emissivity minima in ASTER bands 13 or 14, whereas quartz and microcline minima are centered in shorter wavelength bands (ASTER bands 11 and 12, Fig. 3A), which causes a shift of the restrahlen band envelope toward longer wavelengths with increasing rock mafic content (Lyon, 1964).

In the 0.5–2.5 µm visible near infrared (VNIR) and short wave infrared (SWIR) wavelength region, calcite and ankerite display absorption features at 2.33–2.34 µm and 2.31–2.32 µm, respectively (Fig. 3C). Ankerite is Fe-bearing and forms in a solid solution series with dolomite [$Ca(Fe^{2+},Mg,Mn)(CO_3)_2$] (Mandarino, 1999). Laboratory reflectance spectra of ankeritic carbonatite from Iron Hill, Colorado, indicate that the $CO_3$ absorption feature in ankerite is centered at 2.32 µm (Figs. 3C and 3D).

Some phyllosilicate minerals, such as biotite, chlorite, and phlogopite, display absorption features near 2.32 µm, which may cause ambiguities in distinguishing carbonate minerals from mafic minerals in images with limited spectral resolution and/or low signal:noise (S:N) (Fig. 3C; Hunt, 1977). REE-bearing carbonate minerals and apatite are characterized by narrow $Nd^{3+}$ absorption features, which are centered at specific wavelength positions (Rowan et al., 1986; Rowan and Mars, 2003) (Fig. 3C).

ASTER's multispectral sampling permits discrimination of pixels dominated by a particular mineralogical group, but more specific mineral identification is usually not feasible (Fig. 3D; Rowan and Mars, 2003; Rowan et al., 2006). ASTER spectral reflectance analysis has proven effective for mapping lithologies characterized by ferric-iron and ferrous-iron, Al-OH, Fe, Mg-OH, and $CO_3$ absorption features (Hewson et al., 2005; Rowan and Mars, 2003; Rowan

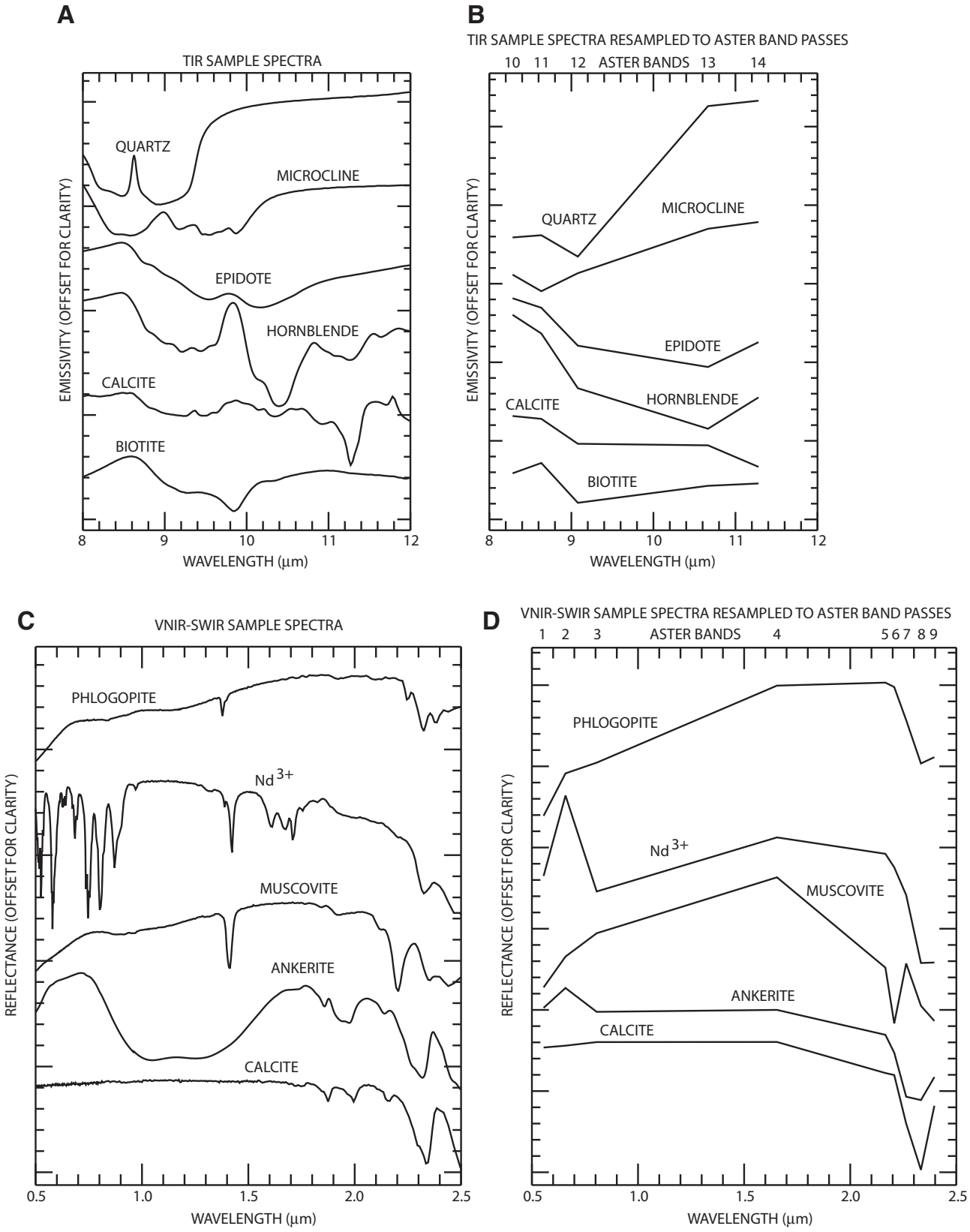


**Figure 3. Comparison of laboratory spectra and the same spectra after resampling to ASTER bandpasses: (A) high-resolution emissivity spectra of important rock-forming minerals; (B) Figure 3A spectra resampled to the ASTER TIR bandpasses (Fujisada, 1995); (C) high-resolution reflectance spectra of several important minerals and neodymium oxide ($Nd^{3+}$) (Clark et al., 1993); vertical lines at 2.20 μm and 2.30 μm are shown for reference; and (D) Figure 3C spectra resampled to the ASTER VNIR+SWIR bandpasses (Fujisada, 1995).**

et al., 2006), and some spectrally subtle differences permit discrimination of calcite from dolomite, and Fe-muscovite from K-muscovite in well-exposed areas (Rowan and Mars, 2003).

## CALIBRATION AND IMAGE PROCESSING

The ASTER instrument acquired data from the Khanneshin study area on July 6, 2001 and the AST_l1b radiance data were downloaded from the Land Processes Distributed Active Archive Center (LP DAAC) at the EROS data center in Sioux Fall, South Dakota. A crosstalk algorithm and radiance correction factors were applied to ASTER SWIR data to correct for anomalies in the SWIR radiance data (Biggar et al., 2005; Iwasaki and Tonooka, 2005; Mars and Rowan, 2006; Mars and Rowan, 2010). The three VNIR bands of ASTER data were co-registered with the six SWIR bands subsequent to spatially resampling the 30 m resolution SWIR data to match the 15 m resolution VNIR data. The atmospheric water-vapor estimate used for calibration of the VNIR+SWIR image was obtained from Moderate Resolution Imaging Spectrometer (MODIS) MOD05_L2 data (Gao and Kaufman, 2003), which were collected simultaneously with the ASTER acquisition, and input into atmospheric correction software to calibrate the nine-band ASTER Level_1B radiance data to reflectance data (ImSpec, 2004). The atmospheric correction algorithm uses radiative transfer code to compensate for atmospheric absorption and scattering effects (Chandrasekhar, 1960).

A sand sample obtained from the study area in the summer of 2009 was used to calibrate ASTER VNIR, SWIR reflectance data (Rowan and Mars, 2003). The sample was measured in the laboratory using an Analytical Spectral Device (ASD) spectrometer, which records 2151 channels throughout the 0.4–2.5 µm wavelength region. The sand spectrum was then resampled to simulate ASTER reflectance VNIR-SWIR data using ASTER bandpasses. The quotient of the ASTER-resampled sand spectrum divided by an ASTER reflectance VNIR-SWIR image spectrum representing the same area was used to rescale the reflectance values (Rowan and Mars, 2003).

The ASTER spectral emittance data evaluated in this study were the standard product (AST_05), which was produced at the LP DACC using the temperature-emissivity separation (TES) algorithm developed by Gillespie et al. (1998). The TIR spectral emittance data were resampled to 15 m resolution and co-registered to the nine-band VNIR+SWIR data. A decorrelation stretch image was compiled from AST_05 bands 12 (red), 11 (green), and 10 (blue) using image analysis software (Gillespie et al., 1986; ITT, 2008).

Minimum noise transform (MNF) analysis was used to reduce noise in the ASTER TIR and SWIR data (Green et al., 1988). MNF data compiled from AST_05 data indicated that MNF TIR bands 1 through 3 contained coherent data while MNF bands 4 and 5 contained noise. Thus, in order to reduce noise in the TIR data an inverse MNF transform using MNF bands 1 through 3 was used to compile a noise-suppressed five band ASTER TIR data set. In addition, MNF analysis of ASTER SWIR data showed that MNF band 6 contained mostly noise; thus an ASTER six-band SWIR data set was compiled using inverse MNF bands 1 through 5, which substantially reduced noise in the SWIR data.

## IMAGE ANALYSIS

### ASTER TIR

Decorrelation-stretch images are an especially effective means of displaying spectral emittance among felsic, mafic, ultramafic, and carbonate rocks (Gillespie et al., 1986). In a typical decorrelation-stretch image in which ASTER band 13 or 14 is displayed in red, band 12 in green, and band 10 in blue, felsic rocks appear red, mafic rocks are blue, and carbonate rocks and vegetation are green (Fig. 4). However, an ASTER band 3/2 ratio map (not shown), which maps the chlorophyll absorption feature at 0.68 µm, did not illustrate any green vegetation in the study area. Thus, the central part of the crater, according to the decor image, is primarily carbonate in composition (green, Fig. 4). The decorrelation stretch image of AST_05 bands 13 (red), 11 (green), and 10 (blue) illustrates that yellow pixels on the north and south sides of the crater contain high band 13 and band 10 values, which are mixtures of felsic (sandstone) and carbonate (carbonatite) rocks (Fig. 4). Pink pixels surrounding the crater in the decorrelation stretch image contain high band 13 and low, approximately equal, band 11 and band 10 values. The pink pixels correspond to the contact metamorphosed sandstone and argillite, which are interpreted as felsic rocks with smaller but equal components of mafic and carbonate rocks (Fig. 4). Blue pixels in the decorrelation-stretch image indicate mafic material and suggest that mafic volcanic rocks and eroded mafic sediment from the volcano cover the northeastern part

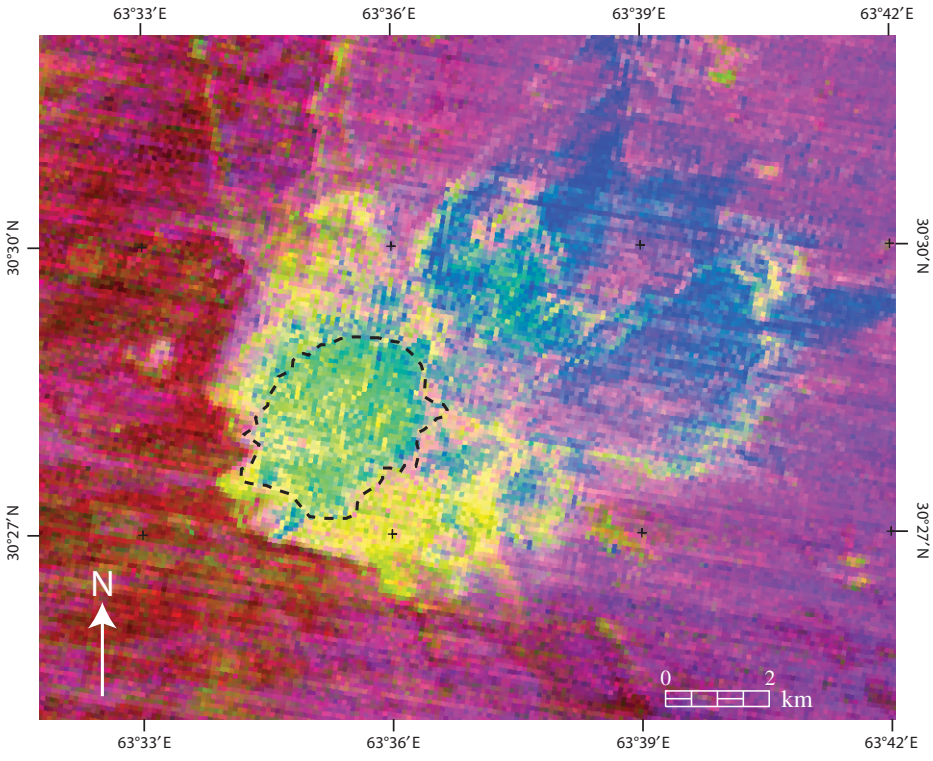


**Figure 4. Decorrelation-stretch ASTER image of the Khanneshin volcano study area (Gillespie et al., 1986). Red—band 13; green—band 12; and blue—band 10. Crater rim highlighted by black-dotted line.**

of the study area (Fig. 4). Purple pixels in the decorrelation-stretch image contain high band 13 and band 10 values, which indicate mixing of mafic and felsic components and suggest that the eastern part of the study area consists primarily of mafic volcanic sediment eroded from the volcano mixed with surrounding quartz-rich eolian and fluvial sediments (Fig. 4). The false color composite image (R = 6, G = 3, B = 1) illustrates that the western part of the plain below Khanneshin is covered by linear eolian sand dunes, which are red in the corresponding decorrelation-stretch image and suggest that the sands are quartz-rich (Figs. 1B and 4).

TIR ratio images are useful for distinguishing certain lithologic groups and identifying pixels for use as reference spectra for subsequent spectral analysis and classification (Rowan et al., 2006). The 14/12 band ratio image is effective for displaying quartzose materials with $SiO_2$ (9.1 µm) spectral absorption whereas the 13/14 band ratio image shows well-exposed carbonate deposits that exhibit weak 11.2 µm spectral absorption (Figs. 5A and 5B, respectively; Rowan et al., 2006). The relative-band-depth (12+14)/13 image (RBD 13) is useful for displaying mafic and ultramafic rocks that exhibit 10.6 µm absorption features (Fig. 5C; Rowan et al., 2006). A lithologic map of quartz-rich, carbonate-rich, and mafic-rich rocks was compiled using the TIR ratio images by displaying only the highest digital numbers (DN) and comparing the pixel distribution of each image with the generalized geologic map and decorrelation stretch image (Figs. 2, 4, and 6). In order to illustrate the proper distribution of rocks and sediment the carbonate lithologic unit compiled from the TIR ASTER band ratio 14/13 is stacked on top of the RBD 13 mafic-rich lithologic unit (Fig. 6). The RBD 13 values are more widespread and correspond to carbonatite and deposits of alluvium, which probably contain mixtures of carbonatite and mafic rock fragments and eolian sand and fluvial sediments (brown, Fig. 6). The quartz-rich lithologic unit compiled from the band ratio 14/12 maps the quartz-rich eolian sands in the western part of the study area (maroon, Fig. 6). Thus, the three lithologic units of the TIR map compiled from the high DN values for the band 14/band 12, band 13/band 14, and RBD 13 show good agreement with the decorrelation-stretch image and the geologic map (Figs. 6, 4, and 2, respectively).

The emittance spectra that correspond to the TIR spectral units illustrate spectral contrast among some of the main lithologies in the study area (Figs. 6 and 7). The quartzose spectrum exhibits intense absorption in band 12 due to quartz (Fig. 7). This feature is also present in

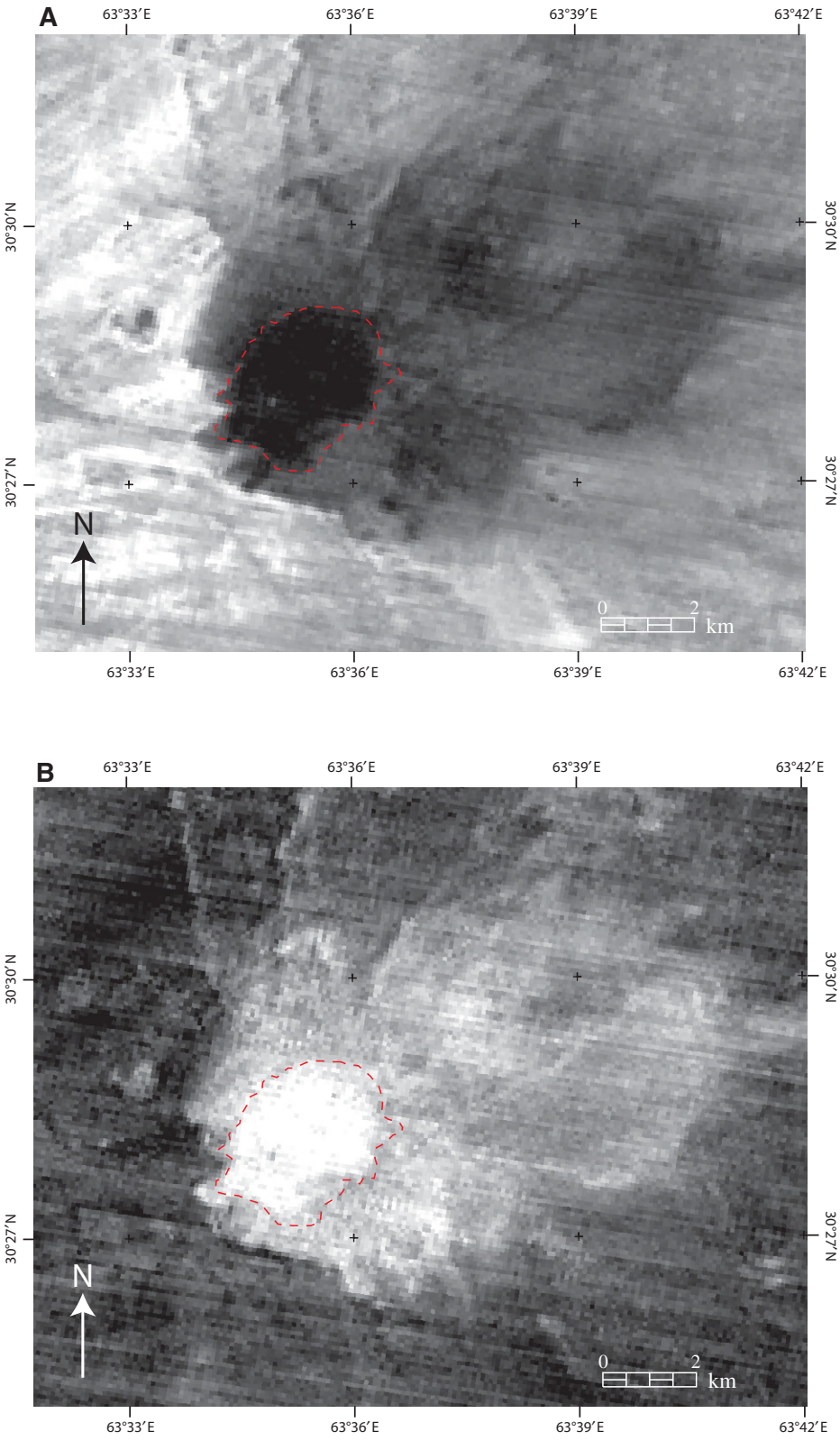


**Figure 5 (*on this and following page*). ASTER TIR ratio images of the Khanneshin volcano study area showing spectral variations caused by lithologic composition differences: (A) band 14/band 12, showing high DN values (bright) caused by quartzose deposits, and low values (dark) in carbonate-rich areas and vegetation concentrations; (B) band 13/band 14, showing high DN values caused by carbonate deposits and green vegetation (none present).**

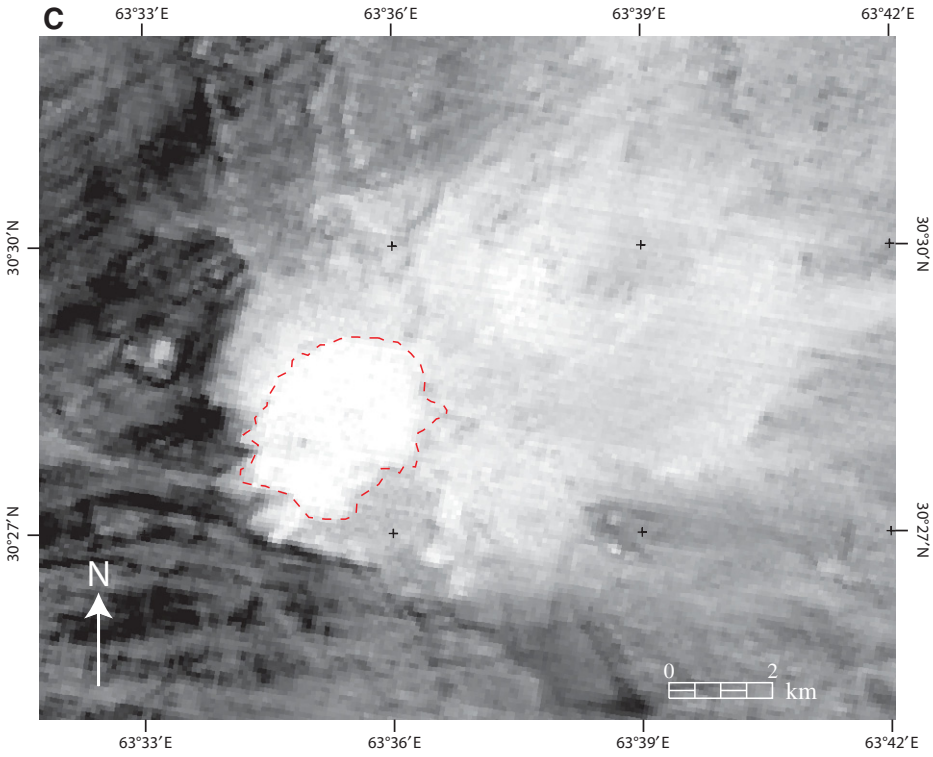


**Figure 5 (*continued*). (C) Relative-band-depth (RBD) image in which ASTER band 13 is the denominator and bands 14 and 12 constitute the numerator, showing carbonate-rich deposits with high DN values and carbonate deposits mixed with silicate material in intermediate values; low DNs represent quartzose deposits. Crater rim highlighted by red-dotted line.**

the carbonatite and carbonatite-mafic-felsic-mix spectra, probably due to the admixture of quartzose sedimentary rocks, either as xenoliths or interlayered siliceous beds (Fig. 7).

## ASTER VNIR-SWIR

### *ASTER SWIR Pixel Purity and Matched Filter Analysis*

Most of the diagnostic spectral absorption features in argillite (clay-rich rock) and carbonatites are in the SWIR region (Hunt, 1977; Rowan and Mars, 2003). In addition to the 2.31–2.33 µm absorption features observed in carbonate-rich rocks, clay-rich rocks, which consist of muscovite or illite (the weathered product of muscovite), exhibit 2.2 µm absorption features (Figs. 3C and 3D). Thus, a pixel purity index (PPI) was performed on the MNF ASTER SWIR data to map spectral endmembers, which are pixels with the most diagnostic spectral absorption features of a specific mineral or mineral groups (Green et al., 1988; Boardman et al., 1995; Rowan et al., 1995; Rowan and Mars, 2003; Rowan et al., 2003). Although PPI was developed for hyperspectral data, ASTER SWIR data have sufficient spectral resolution for defining spectral endmembers (Boardman et al., 1995; Rowan et al., 2003).

In the Khanneshin data set the ASTER SWIR PPI endmember spectra exhibit $CO_3$ and AL-OH spectral absorption features characteristic of ankeritic and calcitic carbonatites, clay-rich (argillite) sandstones, and a mixture of carbonitite and clay-rich sandstone interpreted as agglomerate (Fig. 8). According to the geologic map, the PPI endmember spectrum that is similar to ankeritic carbonatite is from an ankeritic carbonatite flow southeast of the crater and has 2.2, 2.26, and 2.33 µm absorption features (A in Fig. 2; A in Fig. 8). Although intimate mixing may influence mineral abundances, the shape of the SWIR part of the PPI ankeritic spectrum resembles a laboratory spectrum representing equal amounts of ankerite, muscovite, and calcite (Clark, 1999; A in Fig. 9).

The PPI calcitic carbonatite spectrum has weak 2.2 and strong 2.33 µm absorption features (B in Fig. 8). The geologic map indicates that the PPI calcitic spectrum corresponds to calcitic carbonatite rocks in the southern part of the crater (B in Fig. 2). The shape of the SWIR part of this spectrum resembles a laboratory spectrum containing two-thirds calcite and one-third muscovite (B in Fig. 9). In contrast, the PPI ankeritic spectral endmember has greater band 7 absorption than the calcitic carbonatite spectrum due to the ankeritic $CO_3$ absorption at 2.26 µm (Fig. 3D; A and B in Fig. 8). Thus, calcitic carbonatite and ankeritic carbonatite are distinguishable locally in ASTER data because of this subtle spectral shape difference displayed in the SWIR region.

The PPI endmember spectra that have the 2.2 and 2.33 µm absorption features correspond to the southern rim of the crater near the argillite and sandstone–carbonatite contact, where mixing of country and intrusive rocks is most likely (C in Fig. 2). PPI endmember spectra have spectral absorption features characteristic of the agglomerates, which consist of carbonatite (2.33 µm-$CO_3$ spectral absorption), and argillite (muscovite, 2.2 µm-AL-OH absorption) and sandstone (Fig. 3D; C in Fig. 8). The shape of the SWIR part of the PPI agglomerate spectrum resembles a laboratory spectrum representing equal amounts of muscovite and calcite (C in Fig. 9).

The PPI endmember spectrum that has a band 6 absorption feature is consistent with the 2.2 µm spectral absorption feature exhibited in muscovite. The PPI endmember spectrum is located on the northern rim of the crater in the contact aureole rocks that consist of metamorphosed argillite and sandstone (D in Fig. 2; Fig. 8; Fig. 9D). Thus, spectral absorption features associated with muscovite (AL-OH, ASTER band 6), ankerite ($CO_3$, ASTER bands 7 and 8), and calcite ($CO_3$, ASTER band 8) are critical for identification of agglomerates, ankeritic carbonatite, calcitic carbonatite, and argillite-rich sandstones using ASTER SWIR data.

Matched filter classification, which was used with the PPI spectral endmembers, outputs grayscale images with DN pixel score values related to endmember abundance and conformity of image spectra to endmember spectral shapes (Figs. 10A–10D; Farrand, and Harsanyi, 1997; Harsanyi and Chang, 1994). In some cases, however, due to spectral similarity, matched filter mapped the same areas using different PPI spectral endmembers in multiple images (Figs. 10A–10D).

Ankeritic carbonatite rocks mapped with matched filter using the ankeritic PPI endmember spectrum cover the areas north of the crater, within the crater, and southeast of the crater (A in Fig. 8; A, B, and C in Fig. 10A). The ankeritic carbonatite located north and southeast of the crater corresponds to the geologic map and includes the location of the PPI ankeritic carbonatite spectrum (Fig. 2; A in Fig. 8; A and C in Fig. 10A). The ankeritic carbonatite in the crater on the matched filter image is mapped as

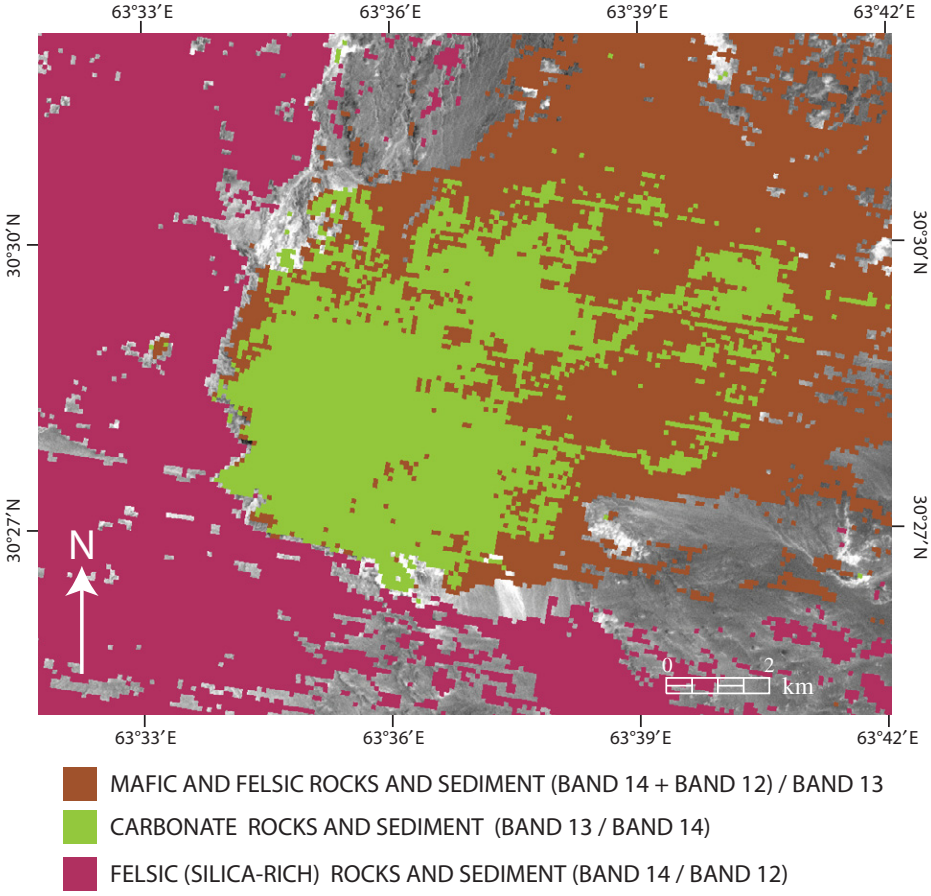


**Figure 6. ASTER TIR lithologic map of the Khanneshin volcano, Afghanistan, compiled from high DN values for each of the ratio images shown in Figure 5A (maroon—band 14/band 12), Figure 5C (brown—RBD13), and Figure 5B (light blue—band 13/band 14). Background image is ASTER band 1.**

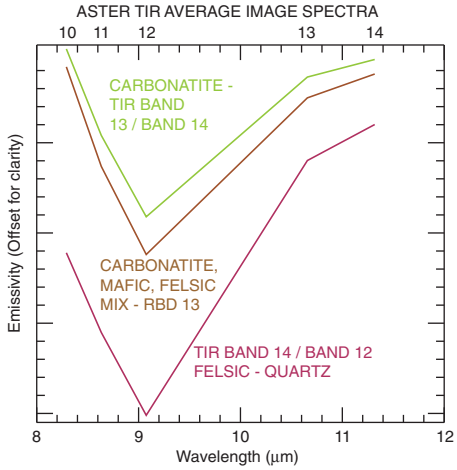


**Figure 7. ASTER TIR image spectra of quartz, carbonatite, and mixture of carbonatite and quartz-rich rock and sediment.**

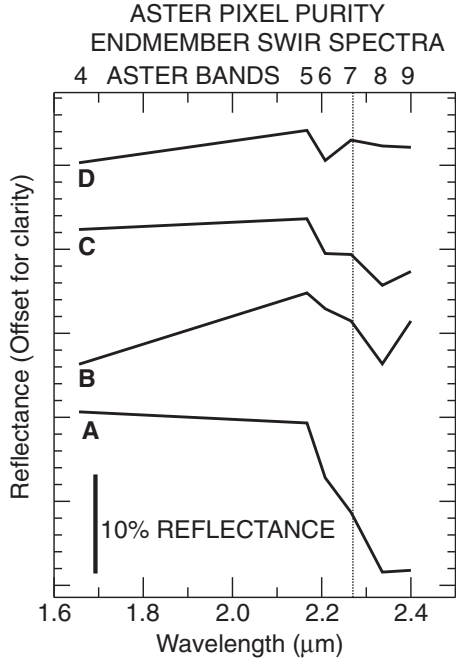


**Figure 8. ASTER pixel purity endmember spectra which according to the geologic map (Fig. 2) are located on: A—ankeritic carbonatite, B—calcitic carbonatite, C—calcitic carbonatite close to the sandstone and argillite rim where agglomerate is more likely to be located, and D—contact metamorphosed sandstone and argillite. Locations of image spectra are shown in Figure 2. The ankeritic carbonatite spectrum A has 2.2, 2.26, and 2.33 μm spectral absorption features caused by ankerite, calcite, and muscovite, the calcitic carbonatite spectrum B has a weak 2.2 and strong 2.33 μm spectral absorption feature caused by muscovite and calcite, the spectrum of agglomerate C has 2.2 and 2.33 μm spectral absorption features of the same intensity caused by muscovite and calcite, and contact-metamorphosed argillite and sandstone D has a 2.2 μm spectral absorption feature caused by muscovite.**

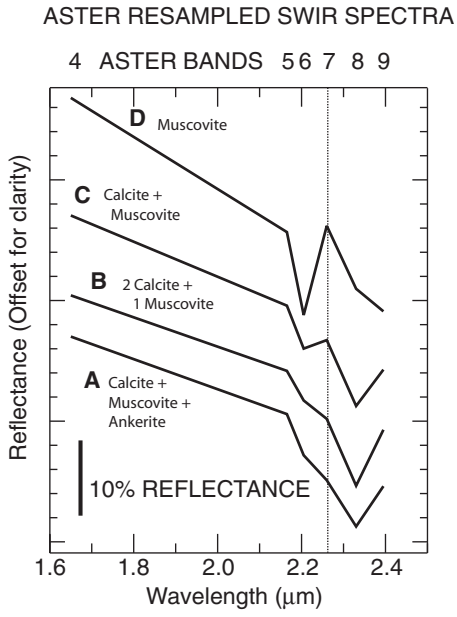


**Figure 9. ASTER resampled sample spectra of A—1 calcite + 1 muscovite + 1 ankerite, B—2 calcite + 1 muscovite, C—1 calcite + 1 muscovite, and D—1 muscovite.**

calcitic carbonatite on the geologic map and the PPI calcitic matched filter image (Fig. 2; B in Fig. 10A; A in Fig. 10B). Spectral analysis of the carbonatite in the crater indicates that there is more intense band 8 absorption than observed in the PPI ankeritic carbonatite spectrum and is therefore interpreted as a mixture of primarily calcitic and smaller amounts ankeritic carbonatite (Figs. 8A and 8B; B in Fig. 10A). Ankeritic carbonatite along the rim of the crater, northeast of the crater, and south of the crater on the geologic map did not map in the ankeritic spectral endmember match filter image (Figs. 2 and 10A). Spectral assessment of these unmapped areas show no significant band 8 (2.33 µm) or band 7 (2.26 µm) absorption features related to ankeritic carbonatite.

Calcitic carbonatite rocks mapped using the calcitic PPI spectrum cover most of the crater, southwest of the crater, and, sporadically, northeast of the crater (B in Fig. 8; A, B, and C in Fig. 10B). The calcitic carbonate rocks illustrated in the matched filter image correspond to calcitic carbonate rocks shown on the geologic map and the position where the PPI calcitic carbonatite spectrum is located (Fig. 2; B in Fig. 2; A and B in Fig. 10B). Calcitic carbonatite deposits shown on the geologic map west, north, and southeast of the crater did not map on the matched filter image (Figs. 2 and 10B). Spectral assessment of the areas not mapped using ASTER data north and southeast of the crater show no significant 2.33 µm absorption feature related to calcite. In addition, the unmapped area west of the crater contains 2.2 and 2.33 µm absorption features which suggest mixing of volcanic carbonate and clay-rich rocks (agglomerate).

Rocks with 2.2 and 2.33 µm absorption features mapped using the agglomerate PPI spectra sporadically cover the crater, the northwest part of the crater rim, and areas west, north, and southeast of the crater (C in Fig. 8; A, B, C, D, and E in Fig. 10C). According to the geologic map all the areas mapped as agglomerate in the matched filter image consist of carbonatite and agglomerate with sandstone except for the northwest crater rim, which is covered by sandstone and argillite and contact-metamorphosed sandstone and argillite. Spectral analysis of areas with high DN values in the matched filter image indicate that the crater and the area west of the crater contain 2.2 and 2.33 µm absorption features consistent with muscovite and illite (AL-OH) from argillite mixed with calcite and ankerite ($CO_3$) from the carbonatite (Fig. 3D; C in Fig. 8; A and C in Fig. 10C). The less extensive areas north and southeast that mapped as agglomerate have spectral characteristics that are similar to the ankeritic carbonatite PPI spectrum (A in Fig. 8; D and E in Fig. 10C).

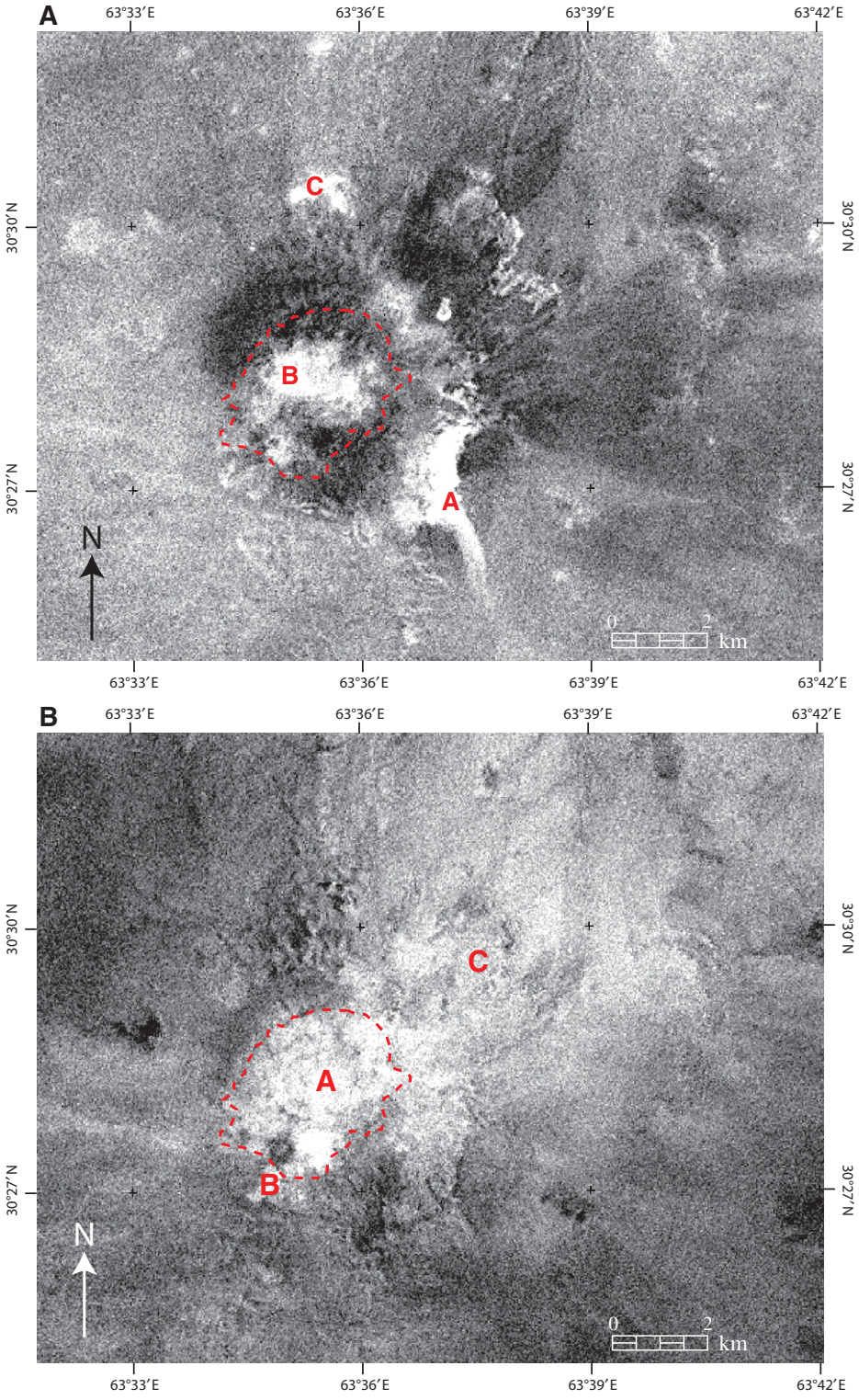


**Figure 10 (*on this and following page*). Matched filter images of the Khanneshin volcano study area compiled from PPI spectra (Fig. 8). Bright areas represent close spectral matches to corresponding PPI spectra. (A) ASTER SWIR matched filter image using the ankeritic carbonatite PPI spectrum; areas A and C contain rocks with spectra similar to ankeritic PPI spectra; area B consists primarily of rocks with spectra that are similar in spectral shape to a mixture of primarily the calcitic PPI spectrum and a smaller amount of the ankeritic PPI spectrum. (B) ASTER SWIR matched filter image using the calcitic carbonatite PPI spectrum; areas A, B, and C are covered with rocks that exhibit spectra similar to calcitic PPI spectra.**

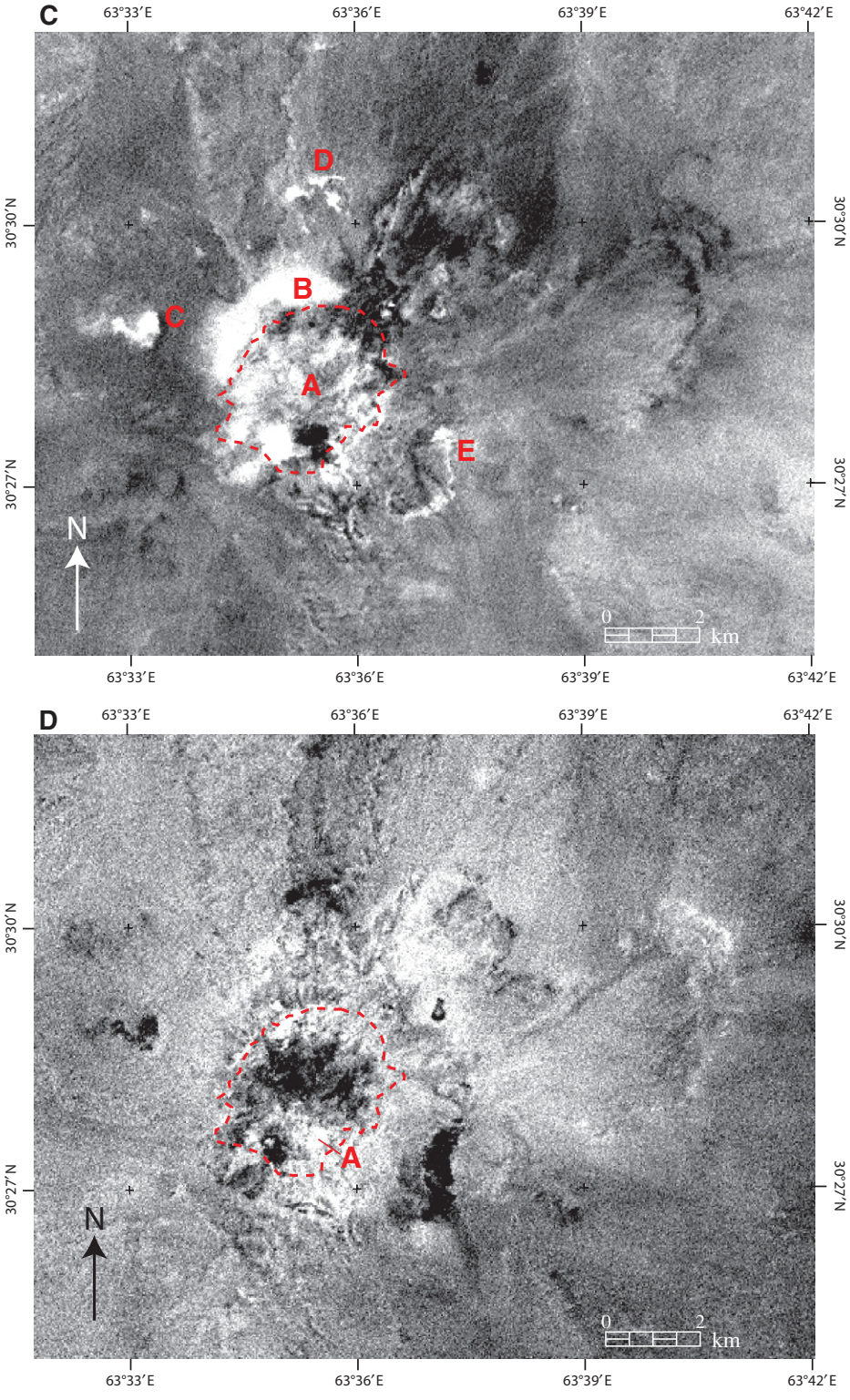


**Figure 10 (*continued*). (C) ASTER SWIR matched filter image using the agglomerate PPI spectrum; areas A and C contain rock that exhibit similar spectral shape to the PPI agglomerate spectrum; spectra from area B have low band 4 reflectance when compared to the PPS agglomerate spectrum; and areas D and E have spectra that are more similar to the ankeritic carbonatite PPI spectrum. (D) ASTER SWIR matched filter image using the argillite and sandstone PPI spectrum; area A contains rock with strong 2.33 µm absorption and weak 2.2 µm absorption. Crater rim highlighted by red-dotted line.**

Rocks with 2.2 µm absorption features mapped using the contact-metamorphosed argillite-sandstone PPI spectrum cover the southern part of the crater, the crater rim, and the areas south and north of the crater (Fig. 10D). According to the geologic map, the ASTER mapped rocks with band 6 absorption consist of calcitic and ankeritic carbonatite, sandstone and argillite, and contact metamorphic rocks. Most of the spectra with high DN values in the matched filter image lack or have a weak 2.33 µm (band 8) absorption feature. The lower spatial coherence of the image compared to the other PPI matched filter images suggests a greater amount of mixed rock types such as carbonatite, and sandstone and argillite. In the southern part of the crater an area with high DN values in the matched filter image exhibits intense band 8 and minor band 6 absorption features and also maps as calcitic carbonatite (A in Fig. 10D; Fig. 10B).

### *Contact Metamorphosed and Iron-Quartz-Rich Rocks*

The circular green pattern of pixels in the ASTER false color composite (R = 6, G = 3, B = 1) image appears to correspond generally to the contact aureole within the polymict sandstone and argillite shown on the geologic map (Figs. 1B and 2). These crater rim rocks have 2.2 and 2.33 µm absorption features and have high DN values in the PPI agglomerate matched filter image (B in Fig. 10C; A in Fig. 11). When compared to other image spectra from the study area, the rocks also have low band 4 reflectance with respect to bands 3 and 5, moderately high band 3 reflectance, and low band 1 reflectance. These spectral characteristics are similar to a mixture of muscovite, chlorite, and epidote (Fig. 3D; A in Fig. 11; Fig. 12). The crater rim rocks have been described in the field as metamorphosed, green, sandstone, and argillite (Alkhazov et al., 1978). Contact metamorphosed clay-rich and basic rocks (hornfels) typically consist of the minerals chlorite, epidote, and muscovite (Yardley, 1989). Chlorite and epidote are green minerals that exhibit a 2.31 µm absorption spectral absorption feature and have relatively low band 4 absorption when compared to other minerals (Figs. 3D and 12). Thus, geologic descriptions and spectral data from the crater rim suggest that the ASTER band 8 absorption feature is caused by chlorite and epidote (FeMg-OH) and the ASTER band 6 absorption is caused by muscovite (ALOH).

On the basis of spectral properties, a relative band depth ratio ((3 + 5)/4), a 3/1 band ratio, and a threshold of band 1 was used in an interactive data language (IDL) logical operator (A) to map the contact metamorphosed crater rim rocks (A in Fig. 11; Fig. 13).

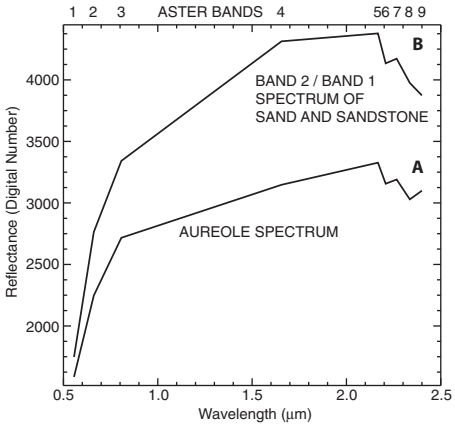


**Figure 11. VNIR-SWIR ASTER spectral averages of spectra consisting of A—the contact metamorphosed argillite and sandstone (contact aureole) unit (Fig. 13; cyan, Figs. 15 and 17) and B—the $Fe^{3+}$ band ratio 2/1 spectral unit (magenta, Figs. 15 and 17).**

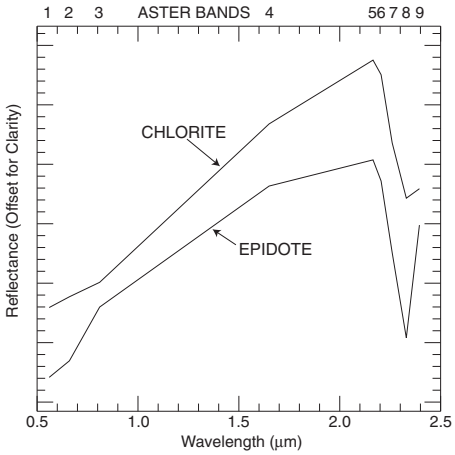


**Figure 12. VNIR-SWIR sample spectra of chlorite and epidote resampled to ASTER bandpasses.**

(A) (float(b3)/b1) gt 1.666 and
(float(b3)/b1) lt 1.7827 and
((float(b3)+b5)/b4) gt 1.876 and b1 lt 1760

lt = less than; gt = greater than;
float = floating point.

Logical operators use band ratios and band thresholds to map spectral shapes (Mars and Rowan, 2006). The logical operator byte image that maps the contact areole rocks matches the pattern of green rocks illustrated in the ASTER false color composite image (R = 6, G = 3, B = 1) and has an averaged spectrum similar

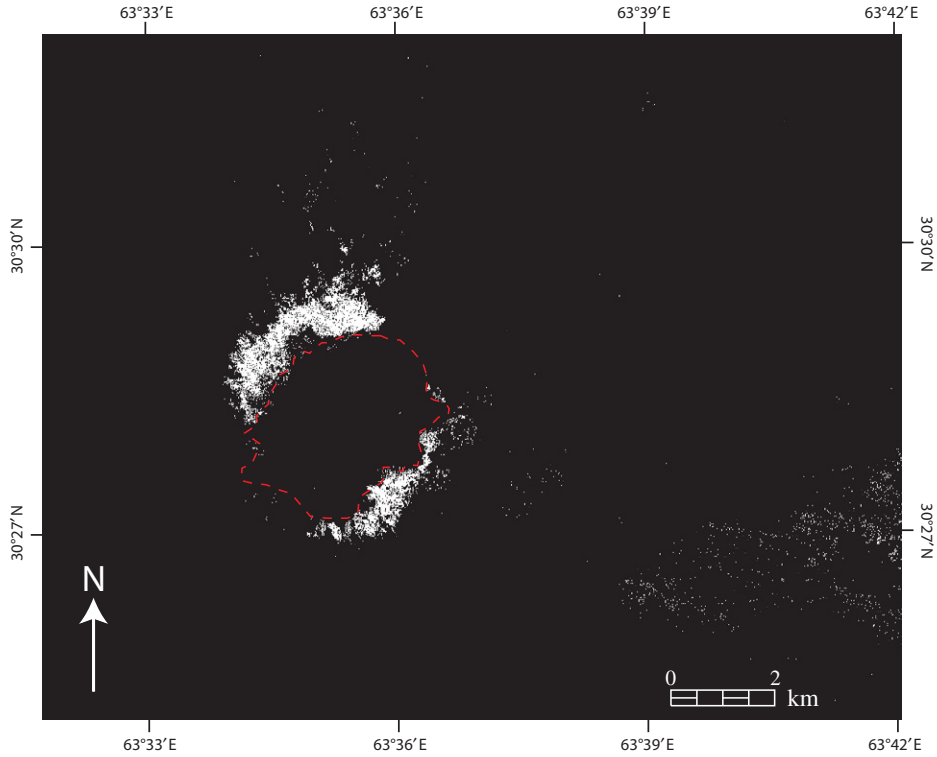


**Figure 13. Logical operator byte image of contact aureole rocks (white) of the Khanneshin volcano area, Afghanistan.**

to chlorite and epidote (Fig. 1B; A in Fig. 11; Figs. 12 and 13).

Iron-rich rocks were mapped using a 2/1 band ratio (Rowan and Mars, 2003). The 2/1 ratio map shows iron-rich rock and sediment south, north, and northwest of the crater (A, B, and C in Fig. 14). Spectra from the iron-rich rocks north and south of the crater exhibit strong $Fe^{3+}$ band 2 and AL-OH band 6 absorption features and very weak band 8 absorption features (B in Fig. 11). The iron-rich rocks south of the crater correspond to sandstone and argillites on the geologic map (Fig. 2; A in Fig. 14). The area north of the crater corresponds to carbonatite on the geologic map although the spectra are more similar to the rocks to the south and suggest that the iron-rich rocks north of the crater are sandstone and argillite (Fig. 2; B in Fig. 14). The TIR decorrelation stretch image, however, shows the iron-rich deposits near the north and south sides of the crater as a mixture of felsic and carbonate rocks (Fig. 4; A and B in Fig. 14). The 2/1 band ratio image also illustrates northeast-trending linear patterns of iron-rich sediments northwest of the crater that exhibit spectra with high VNIR-SWIR reflectance, and very weak 2.2 μm band 6 absorption (Fig. 1B; B in Fig. 11; C in Fig. 14). The high VNIR-SWIR reflectance suggests that the deposits are quartz-rich and the weak 2.2 μm spectral absorption indicates that the deposits contain a small amount of muscovite or illite. Thus, the deposits northwest of the crater are interpreted as iron-rich eolian sand dunes on the basis of spectral characteristics and geomorphology (C in Fig. 14).

### *ASTER VNIR-SWIR and ASTER VNIR-SWIR-TIR Mineral and Rock-Type Maps*

An ASTER VNIR-SWIR mineral and rock-type map was produced by threshholding each matched filter image and the 2/1 band ratio image to the highest DN values that best conform to the shape of PPI endmember spectra and high band 2 and 1 separation, respectively (Figs. 8, 10, 14, and 15). In addition, the contact aureole rocks, mapped using the logical operator, were added to the ASTER VNIR-SWIR mineral and rock-type map. The spectral accuracy for each ASTER VNIR-SWIR spectral unit was checked by comparing the spectral average of each unit to the PPI endmember spectra, spectra from image data with high DN values on the 2/1 band ratio map, or spectra located in the contact aureole according to the geologic map (Figs. 2, 8, 11, 13, 15, and 16).

Each spectral unit is placed in a vector layer and stacked to form the ASTER VNIR-SWIR

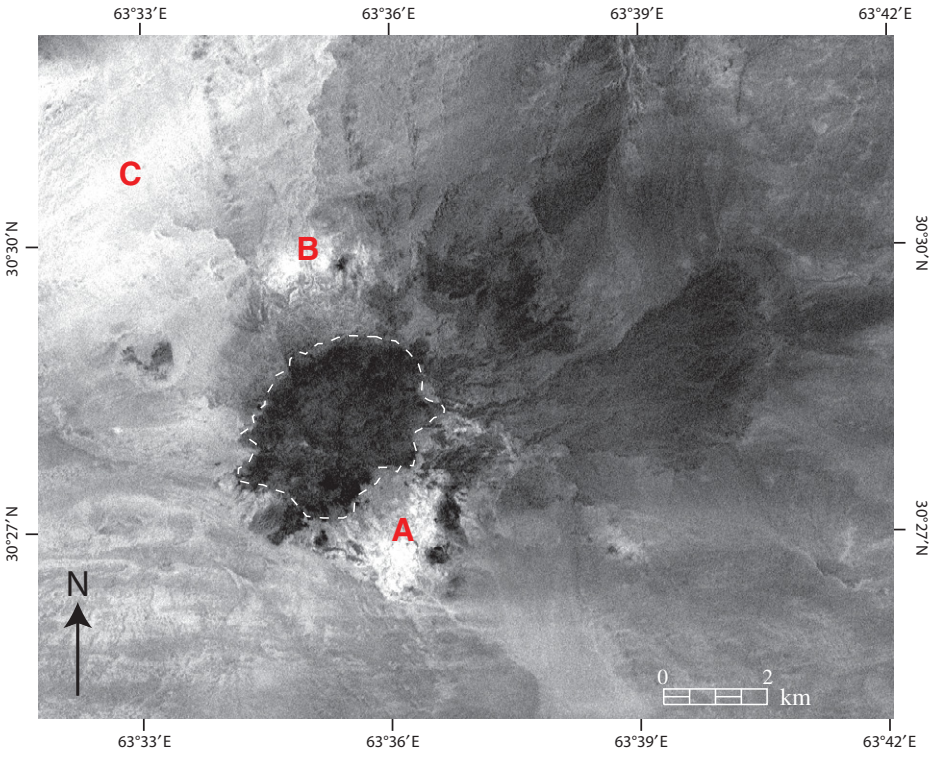


**Figure 14. ASTER band ratio 2/1 of the Khanneshin volcano area, Afghanistan. Bright areas A, B, and C indicate high $Fe^{3+}$ absorption. Crater rim highlighted by white-dotted line.**

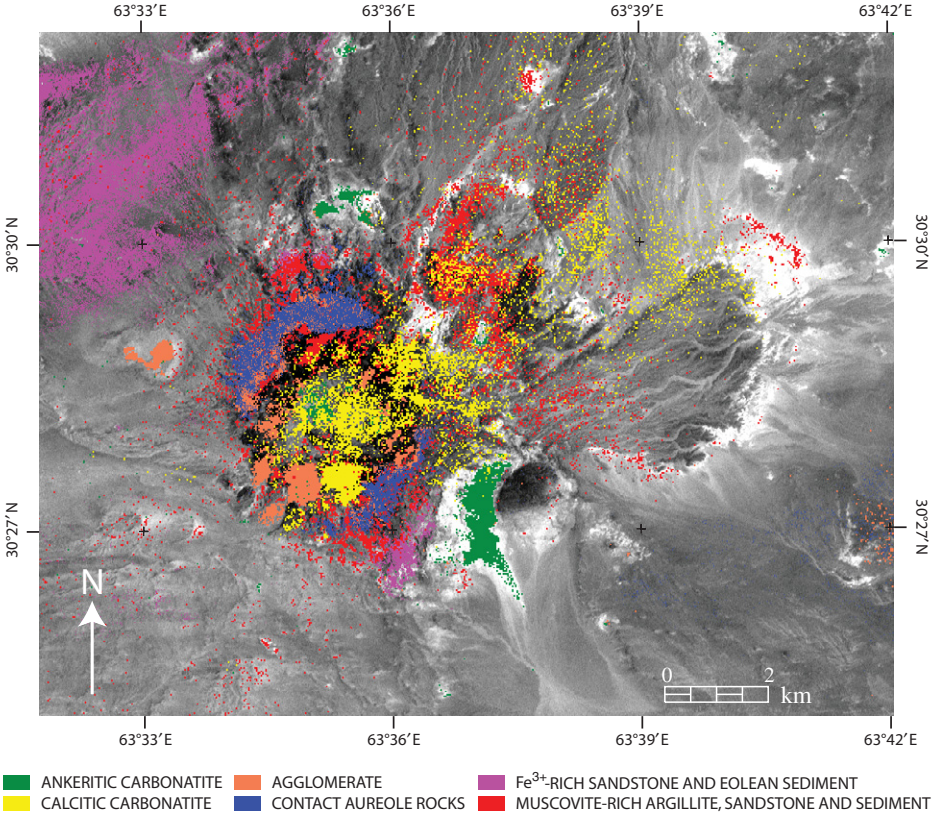


**Figure 15. ASTER VNIR-SWIR mineral and rock-type map of the Khanneshin volcano area, Afghanistan. Background image is ASTER band 1.**

mineral and rock-type map. Some mineral and rock-type units map the same area due to similarity of spectral properties. A proper stacking order of the mineral and rock-type spectral units corrected this problem by placing a spectral unit that correctly mapped the spectral properties of an area over a unit that had mapped rocks or minerals with slightly different spectral properties for the same area. The stacking order of the ASTER mineral and rock-type spectral units from base to top is (1) iron-quartz-rich rocks and sediment; (2) agglomerate; (3) ankeritic, carbonatite; (4) muscovite-rich argillite, sandstone and sediment; (5) calcitic carbonatite; and (6) contact aureole rocks. Proper stacking of spectral unit layers results in a mineral and rock-type map that matches the spectral properties of the ASTER data and the lithologic units shown on the geologic map (Figs. 2 and 15).

The ASTER VNIR-SWIR mineral and rock-type map shows that most of the rocks within the crater and northeast of the crater consist of calcite-rich rocks interpreted as calcitic carbonatite (yellow, Fig. 15). The map also illustrates that the crater contains a small amount of ankeritic carbonatite with large ankeritic carbonatite flows located southeast and north of

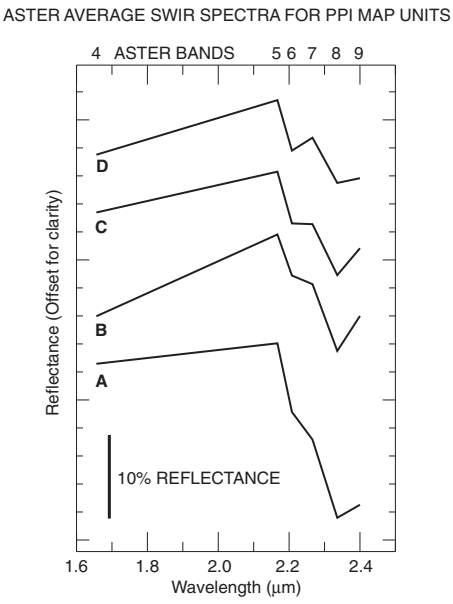


**Figure 16. VNIR-SWIR ASTER spectral averages of spectra consisting of A—the ankeritic carbonatite spectral unit (dark green, Figs. 15 and 17); B—the calcitic carbonatite spectral unit (yellow, Figs. 15 and 17); C—the agglomerate spectral unit (orange, Figs. 15 and 17); and D—the argillite and sandstone spectral unit (red, Figs. 15 and 17).**

the crater (dark green, Fig. 15). Agglomerate is situated primarily along the inside of the crater rim and there is a large isolated deposit west of the crater (orange, Fig. 15). The crater rim consists primarily of metamorphosed argillite and sandstone and less laterally extensive agglomerate (blue and orange, respectively, Fig. 15). Muscovite-rich rocks and sediments cover areas along the rim of the crater, northeast of the crater, and east of the crater on the alluvial fan (red, Fig. 15). Iron-rich ($Fe^{3+}$) rocks cover areas north and south of the crater and iron-rich eolian sand dunes cover the area northwest of the volcano (magenta, Fig. 15).

A combination VNIR-SWIR and TIR mineral and rock-type map was compiled by overlaying the VNIR-SWIR units on top of the TIR units (Fig. 17). The TIR data map more laterally extensive carbonate, quartz -rich, and mixed carbonate and quartz-rich rocks than the VNIR-SWIR data (Figs. 6 and 15). In addition, quartz-rich rocks that exhibit $SiO_2$ absorption observed in the TIR data can be mapped, which is not possible using the VNIR-SWIR data because quartz VNIR-SWIR spectra are featureless. In contrast, the VNIR-SWIR data offer more diverse classification and higher spatial resolution of mineral groups than the TIR data (Figs. 6 and 15). With the exception of the $Fe^{3+}$-rich unit interpreted as argillite and sandstone from the VNIR-SWIR spectra and sandstone argillite and carbonatite from the TIR spectra, all the VNIR-SWIR units map within the more generalized TIR units, providing a cross correlation between the VNIR-SWIR and TIR map units. Thus, the VNIR-SWIR and TIR data complement each other and produce a mineral and rock-type map that is collectively more similar to the geologic map than mineral and rock-type maps compiled using either VNIR-SWIR or TIR data (Figs. 6, 15, and 17).

## SUMMARY AND CONCLUSIONS

ASTER VNIR-SWIR data were used to map minerals and rock types on the basis of their spectral absorption features and their association with a preexisting geologic map of the area (Fig. 2). Carbonatite rocks on the geologic map were defined in ASTER images based on $CO_3$ absorption in the 2.32–2.33 and 11.2 µm regions (Figs. 5, 10, and 15). Calcitic carbonatite was distinguished from ankeritic carbonatite in the ASTER SWIR by the slight shift of the $CO_3$ absorption feature to 2.26 µm in the ankeritic spectrum, but some areas of ankeritic carbonatite illustrated on the geologic map were not identified in the ASTER image (Figs. 2, 8, and 16). Rocks with ASTER bands 6 and 8 absorption in the crater were identified as agglomerates that contain calcite and muscovite. Rocks with ASTER bands 4, 6, and 8 absorption along the crater rim were identified as metamorphosed argillite and sandstone that probably contain chlorite, epidote, and muscovite. Rocks that exhibit a 2.2 µm absorption feature were interpreted as muscovite and possibly illite-rich argillite and sandstone or contact metamorphosed argillite and sandstone. Iron-rich ($Fe^{3+}$) sand and sandstone possibly mixed with carbonate rock that lie north and south of the crater rim have a 0.53 µm spectral absorption feature that was mapped using an ASTER band ratio of 2/1.

The widespread distribution of carbonate rocks within the Khanneshin volcano were also indicated by $CO_3$ absorption in ASTER TIR band 14 which causes high ASTER band 13/band 14 values (Figs. 5B and 6). Laterally extensive silica-rich rock and eolian sediment were mapped in the western part of the study area using the ASTER band ratio 14/12 which highlights $SiO_2$ absorption at 9.4 µm (Figs. 5A and 6). A mixture of carbonatite and quartz-rich rock and sediment was mapped in

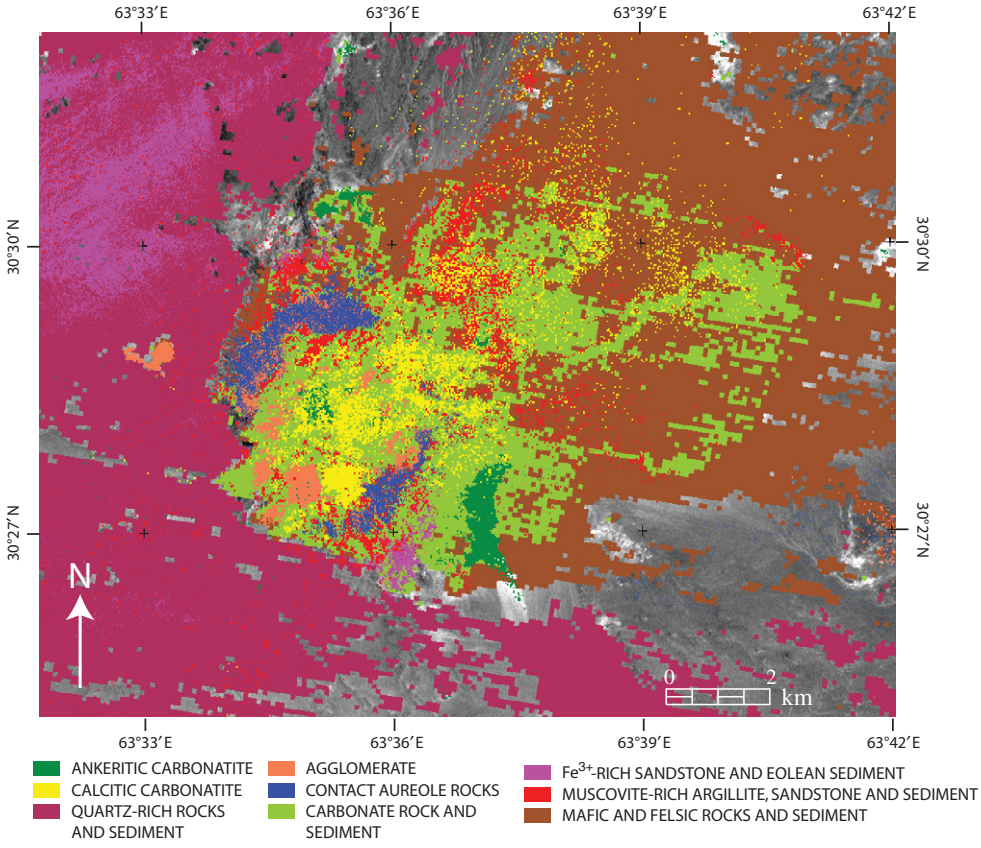


**Figure 17. Combined ASTER VNIR-SWIR-TIR mineral and rock-type map of the Khanneshin volcano area, Afghanistan. Background image is ASTER band 1.**

the northeastern part of the study area using an ASTER TIR relative band depth ratio of (12+14)/13 (Figs. 5C and 6).

Mineral and rock-type maps were compiled from VNIR, SWIR, and TIR data. The VNIR-SWIR mineral and rock-type map illustrates detailed distribution of calcitic and ankeritic carbonatites, as well as agglomerates, contact metamorphosed rocks, argillite and sandstone, and iron-rich sandstone (Fig. 15). The TIR mineral and rock-type map illustrates widespread silica, carbonate, and mafic-rich rock and sediment (Fig. 6). The VNIR, SWIR, and TIR mineral and rock-type map combines more laterally extensive TIR spectral units with a greater variety of VNIR-SWIR spectral units that is collectively more similar to the geologic map than mineral and rock-type maps compiled using either VNIR-SWIR or TIR data.

Thus, ASTER data, carefully calibrated and analyzed according to established methods, provide image-based maps of rocks and minerals that are consistent with available geologic mapping information for the Khanneshin area. The methods used to calibrate the data and map the rocks and minerals in this study are well documented and have been used in other geologic remote sensing studies (Mars and Rowan, 2006; Mars and Rowan, 2010; Rowan and Mars, 2003; Rowan et al., 2003; Rowan et al., 2006). The ASTER mineral and rock-type maps illustrate a surficial elliptical pattern of carbonate rocks associated with contact-metamorphosed and mafic rocks that can be used as an exploration guide for discovering new carbonatite deposits. In addition, these ASTER mapping methods will assist in exploration of important deposits such as REE and radioactive elements, which are typically associated with carbonatite deposits and adjacent rocks.

**ACKNOWLEDGMENTS**

I would like to thank Bernard Hubbard, Jim Crowley, and Mike Taylor for their editorial reviews, which greatly improved the manuscript. Most importantly, I want to thank my mentor and colleague Larry Rowan for his insight, friendship, and collaboration. The geologic remote sensing community has lost a great intellect and researcher, and I have lost a great friend.

**REFERENCES CITED**

Alkhazov, V.Yu., Atakishiyev, Z.M., and Azimi, N.A., 1978, Geology and mineral resources of the early Quaternary Khanneshin carbonatite volcano (Southern Afghanistan): International Geology Review, v. 20, no. 3, p. 281–286, doi: 10.1080/00206817809471382.

Biggar, S.F., Thome, K.J., McCorkel, J.T., and D'Amico, J.M., 2005, Vicarious calibration of the ASTER SWIR sensor including crosstalk correction: Proceedings International Society Optical Engineering, v. 5882, p. 588,217.

Boardman, J.W., Kruse, F.A., and Green, R.O., 1995, Mapping target signatures via partial unmixing of AVIRIS data: Proceedings of the Fifth JPL Airborne Earth Science Workshop, JPL Publ. 95–01: Pasadena, California, Jet Propulsion Laboratory, p. 23–26.

Bowers, T.L., and Rowan, L.C., 1996, Lithologic mapping of the Ice River Alkaline Complex, British Columbia, Canada, using airborne visible/ infrared imaging spectrometer data: Photogrammetric Engineering and Remote Sensing, v. 62, no. 12, p. 1379–1385.

Castor, S.B., 1991, Rare earth deposits in the southern great basin, geology and ore deposits of the Great Basin, Reno: Geological Society of Nevada, p. 523–528.

Chandrasekhar, S., 1960, Radiative transfer: New York, Dover Publications, 393 p.

Clark, R.N., 1999, Spectroscopy of rocks and minerals, and principles of spectroscopy, *in* Rencz, A.N., ed., Remote Sensing for the Earth Sciences, Manual of Remote Sensing (3rd edition): New York, John Wiley and Sons Inc., p. 3–58.

Clark, R.N., Swayze, G.A., Gallagher, A.J., King, T.V.V., and Calvin, W.M., 1993, The U.S. Geological Survey, digital spectral library: Version 1: 0.2 to 3.0 microns: U.S. Geological Survey Open-file Report 93–592.

Farrand, W.H., and Harsanyi, J.C., 1997, Mapping the distribution of mine tailings in the Coeur D'Alene River Valley, Idaho area through the use of a Constrained Energy Minimization technique: Remote Sensing of Environment, v. 59, p. 64–76, doi: 10.1016/S0034-4257(96)00080-6.

Fujisada, H., 1995, Design and performance of ASTER instrument: Proceedings of SPIE, the International Society for Optical Engineering, v. 2583, p. 16–25.

Gao, B.C., and Kaufman, Y.J., 2003, Water vapor retrivals using Moderate Resolution Imaging Spectroradiometer (MODIS) near-infrared channels: Journal of Geophysical Research, v. 108, no. D13, p. 4389, doi: 10.1029/2002JD003023.

Gillespie, A.R., Kahle, A.B., and Walker, R.E., 1986, Color enhancement of highly correlate images. I. Decorrelation and HSI contrast stretches: Remote Sensing of Environment, v. 20, p. 209–235, doi: 10.1016/0034-4257(86)90044-1.

Gillespie, A.R., Matsunaga, T., Rokugawa, S., and Hook, S.J., 1998, Temperature and emissivity from Advanced Spaceborne Thermal Emission and Reflection Radiometer (ASTER) images: IEEE Transactions on Geoscience and Remote Sensing, v. 36, p. 1113–1126, doi: 10.1109/36.700995.

Green, A.A., Berman, M., Switzer, B., and Craig, M.D., 1988, A transformation for ordering multispectral data in terms of image quality with implications for noise removal: IEEE Transactions on Geoscience and Remote Sensing, v. 26, no. 1, p. 65–74, doi: 10.1109/36.3001.

Harsanyi, J.C., and Chang, C., 1994, Hyperspectral image classification and dimensionality reduction: An orthogonal subspace projection approach: IEEE Transactions on Geoscience and Remote Sensing, v. 32, p. 779–785, doi: 10.1109/36.298007.

Hewson, R.D., Cudahy, T.J., Mizuhiko, S., Ueda, K., and Mauger, A.J., 2005, Seamless geological map generation using ASTER in the Broken Hill-Curnamona Province of Australia: Remote Sensing of Environment, v. 99, p. 159–172, doi: 10.1016/j.rse.2005.04.025.

Hunt, G.R., 1977, Spectral signatures of particulate minerals in the visible and near infrared: Geophysics, v. 42, no. 3, p. 501–513, doi: 10.1190/1.1440721.

ImSpec LLC, 2004, ACORN 5.0 tutorial manual: Pasadena, California, ImSpec, 143 p. (http://www.imspec.com).

ITT, 2008, The Environment for Visualizing Images (ENVI) software: Boulder, Colorado, ITT Visual Information Solutions (http://www.ittvis.com/ProductServices/ENVI.aspx).

Iwasaki, A., and Tonooka, H., 2005, Validation of a crosstalk correction algorithm for ASTER/SWIR, Geoscience and Remote Sensing: IEEE Transactions, v. 43, no. 12, p. 2747–2751.

Le Bas, M.J., 1977, Carbonatite-nephelinite volcanism: London, John Wiley and Sons, 347 p.

Lyon, R.J.P., 1964, Evaluation of infrared spectrophotometry for compositional analysis of lunar and planetary soils, II: NASA Contractor Report. NASA CR, United States, National Aeronautics and Space Administration, p. 100.

Mandarino, J.A., 1999, Fleischer's glossary of mineral species 1999: Tucson, Arizona, The Mineralogical Record Inc.

Mars, J.C., and Rowan, L.C., 2006, Regional mapping of phyllic- and argillic-altered rocks in the Zagros magmatic arc, Iran, using Advanced Spaceborne Thermal Emission and Reflection Radiometer (ASTER) data and logical operator algorithms: Geosphere, v. 2, p. 161–186, 2 plates.

Mars, J.C., and Rowan, L.C., 2010, Spectral assessment of new ASTER SWIR surface reflectance data products for spectroscopic mapping of rocks and minerals: Remote Sensing of Environment, v. 114, p. 2011–2025, doi: 10.1016/j.rse.2010.04.008.

Olson, J.C., Shawe, D.R., Pray, L.C., and Sharp, W., 1954, Rare-earth mineral deposits of the Mountain Pass, District, San Bernardino County, CA: U.S. Geological Survey Professional Paper, v. 261, p. 1–75.

Rowan, L.C., Collins, W.E., Kingston, M.K., and Crowley, J.K., 1984, Spectral reflectance of the carbonatite complexes at Mountain Pass, California and Iron Hill, Colorado: Summary, *in* Proceedings of the Third Thematic Conference on Remote Sensing for Exploration Geology, Colorado Springs, Colorado, 16–19 April 1984, vol. 1, p. 217–218.

Rowan, L.C., Kingston, M.K., and Crowley, J.K., 1986, Spectral reflectance of carbonatite and related alkalic igneous rocks: Selected samples from four North American localities: Economic Geology and the Bulletin of the Society of Economic Geologists, v. 81, p. 857–871.

Rowan, L.C., Bowers, T.L., Crowley, J.K., Anton-Pacheco, C., Gumiel, P., and Kingston, M.J., 1995, Analysis of Airborne Visible-Infrared Imaging Spectrometer (AVIRIS) data of the Iron Hill, Colorado, carbonatite-alkalic igneous rock complex: Economic Geology and the Bulletin of the Society of Economic Geologists, v. 90, p. 1966–1982.

Rowan, L.C., 1997, Remote sensing studies of the Mountain Pass, California and Iron Hill, Colorado carbonatite complexes: Summary: Global Tectonics and Metallogeny, v. 6, no. 2, p. 119–123.

Rowan, L.C., 1998, Analysis of simulated advanced spaceborne thermal emission and reflection (ASTER) radiometer data of the Iron Hill, Colorado, study area for mapping lithologies: Journal of Geophysical Research, v. 102, n. D24, p. 32,292–32,306.

Rowan, L.C., and Mars, J.C., 2003, Lithologic mapping in the Mountain Pass, California area using Advanced Spaceborne Thermal Emission and Reflection Radiometer (ASTER) data: Remote Sensing of Environment, v. 84, p. 350–366, doi: 10.1016/S0034-4257(02)00127-X.

Rowan, L.C., Hook, S.J., Abrams, M.J., and Mars, J.C., 2003, Mapping hydrothermally altered rocks at Cuprite, Nevada, using the Advanced Spaceborne Thermal Emission and Reflection Radiometer (ASTER), a new satellite-imaging system: Economic Geology and the Bulletin of the Society of Economic Geologists, v. 98, no. 5, p. 1019–1027.

Rowan, L.C., Mars, J.C., and Simpson, C.J., 2006, Lithologic mapping of the Mordor, Northern Territory, Australia ultramafic complex using Advanced Spaceborne Thermal and Reflection Radiometer (ASTER) data: Remote Sensing of Environment, v. 99, p. 105–126, doi: 10.1016/j.rse.2004.11.021.

Watson, K., Rowan, L.C., Bowers, T.L., Anton-Pacheco, C., Gumiel, P., and Miller, S.H., 1996, Lithologic analysis from multispectral thermal infrared data of the alkalic rock complex at Iron Hill, Colorado: Geophysics, v. 61, no. 3, p. 706–721, doi: 10.1190/1.1443998.

Yardley, B.W.D., 1989, An Introduction to Metamorphic Petrology: New York, Longman Scientific and Technical, 248 p.

Manuscript Received 20 July 2010
Revised Manuscript Received 13 September 2010
Manuscript Accepted 15 September 2010